# Aquatic plant inspired hierarchical artificial leaves for highly efficient photocatalysis

5 authors, including:

Jian Liu
Huawei Technologies
317 PUBLICATIONS   6,869 CITATIONS

SEE PROFILE

Qiang Yang
University of Electronic Science and Technology of China
58 PUBLICATIONS   2,221 CITATIONS

SEE PROFILE

Mingzhu Li
Chinese Academy of Sciences
159 PUBLICATIONS   8,459 CITATIONS

SEE PROFILE

Yanlin Song
Chinese Academy of Sciences
738 PUBLICATIONS   37,753 CITATIONS

SEE PROFILE

## PAPER

# Aquatic plant inspired hierarchical artificial leaves for highly efficient photocatalysis†

Jian Liu,‡ Qiang Yang,‡ Wentao Yang, Mingzhu Li* and Yanlin Song*

The natural leaf provides a superior template for engineering the artificial leaf in order to perform light energy conversion. To adapt to the aquatic environments, the aquatic plant leaves usually are thin and soft with excellent mass transportation and light-harvesting capability. In this report, the aquatic leaf is directly employed as a template to construct bioinspired hierarchical photocatalyst while mesoporous directing agent act as a second template. The dual templates consequently ensure the obtained $TiO_2$ with optimal light harvesting structure, high surface area and excellent mass transportation, which contribute to improve photocatalytic capability. Specially, $SiO_2$ is also introduced to form $TiO_2$–$SiO_2$ composite in the final hierarchical replica in order to improve the stability of mesostructures, perfect replication of leaves' fine structures and the dye adsorption capability for facilitating photodegradation. Consequently, the photocatalytic activity of the as-synthesized leaf replicas in the photodegradation of methylene blue is *ca.* 3 times higher than that of P25, and one order of magnitude higher than that of common nanocrystalline $TiO_2$, under commercial black lamp irradiation.

## Introduction

Photocatalysis provides human beings a convenient and clean method to store solar energy in energy rich molecules such as hydrogen produced from solar water splitting and organics conversed from carbon dioxide.[1–3] To date, great efforts have been paid to improve the efficiency of the photocatalysis, such as surface area enhancement,[4,5] new photocatalytic materials preparation,[6,7] elements doping[8–12] and light enrichment structure construction.[13–15] Recently, much attention has been attracted to construct light-harvesting structures, taking photonic crystals and bio-template structures as examples.[16–21] Photonic crystals are able to enhance light harvesting *via* slow photons.[22,23] Nevertheless, the structure dimensions in wavelength scale, restrict photonic crystals from a large surface area structure, in comparison with mesoporous structures.[18] Nowadays, artificial leaves are focused on to improve photocatalytic performance by utilizing the excellent light harvesting capacity of natural leaves.[20,21,24] For example, the artificial terrestrial leaves fabricated by Zhou *et al.* showed 3.3 times

the rate in splitting water, higher than that of P25, a commercial $TiO_2$ nanocrystalline, due to light focusing of palisade structures, light scattering of spongy structures, and nitrogen doping.[20] However, the structures destruction and surface area reduction during the mimicking process may reduce the light harvesting ability of artificial leaves in comparison with the natural leaves. Herein, we fabricated an artificial $TiO_2$ leaf with macro/mesopores derived from the dual template of aquatic plant leaves and surfactants. The as-prepared $TiO_2$–$SiO_2$ (Ti–Si) hierarchical artificial leaf showed *ca.* 3 times higher than P25 and *ca.* 20 times higher than ordinary $TiO_2$ nanocrystalline in photodegrading Methylene blue (MB) under UV light.

Aquatic photosynthesis, the biological conversion of light energy to chemical energy in the aquatic environment, has provided 40% amount of energy for nearly all life on earth.[25] Being in an underwater environment, the aquatic plant leaf has actually generated many interesting and essential adaptations, ranging from the level of organelles (macroscopic morphology) down to that of molecules (microscopic structure), for special aquatic conditions.[26] The aquatic plant leaf is usually thin, soft and even transparent, which makes them easily access light and mass interchange with surroundings. The macroscopic morphology adaptation of the epidermal cells in the surface of leaves serves the purpose of fully focusing the incident light onto the leaves. Consequently, the light can be effectively trapped within plant tissues. The synergetic effect of light concentration by the leaves epidermal cells and the light scattering of plant tissues contributes to the light harvesting in the interior of the leaf.[27] As known, most of photocatalytic reactions

are performed in aquatic solution, where there is low light intensity.[25] In this case, the aquatic plant leaves provide a superior alternative from their terrestrial counterparts.

In this paper, *Vallisneria*, a typical aquatic grass, was adopted as a bio-template to obtain the artificial leaves for photocatalysis. The leaf templates are able to focus the light under the water and scatter the light enriched in the artificial leaves, hence boosting the photocatalytic performance. Due to the partial loss of delicate structures in the original leaves during mimicking process, we put forward a solution of introducing mesoporous structures into the leaf replicas to compensate the shortage.[28,29] The mesoporous structures are prepared by utilizing the poly(ethylene glycol)-poly(propylene glycol)-poly(ethylene glycol) (P123) as a mesoporous template and $SiO_2$ as a mesoporous stabilizer. The mesoporous structures can further enlarge the surface area and enhance the dye adsorption capability.[13,30] The replicas derived from the *Vallisneria* leaves had effective light harvesting ability underwater. In addition, the macro/mesoporous hierarchical structures were able to facilitate the mass transportation. Therefore, the as-prepared hierarchical artificial photocatalytic leaf showed high photocatalytic efficiency in photodegrading MB under UV irradiation.

## Experiment section

### Pretreatment

Before the fixation procedure, the fresh aquatic plant samples were rinsed with deionized water carefully several times to remove the surface adsorbed plankton. Afterwards, the leaves were treated with 2.5% glutaraldehyde/phosphate buffered saline (PBS; pH = 7.2) solution at 4 °C for one day for the fixation of cells and tissues. The fixed samples were rinsed in the same buffer solution and dehydrated in a graded ethanol series (10%, 20%, 30%, 50%, and 70%, respectively). For SEM observation, the fixed samples were further critical point dried with $CO_2$ and then sputter-coated with a thin layer of gold. For viewing of leaves cross-sectional anatomy, fully dehydrated samples were frozen in liquid nitrogen and fractured manually using tweezers.

### Synthesis of Ti–Si oxide and $TiO_2$ sol

In a typical synthesis, 1.0 g of P123 was dissolved in 30 g of ethyl alcohol, followed with slowly adding 1.8 g of hydrochloric acid with vigorous stirring. The reaction vessel was kept stirring for 3 hours at 40 °C, then 2.34 g of TIPO and 0.434 g of TEOS were added with vigorous stirring for another 5 hours at 40 °C. The obtained colorless transparent solution was allowed to undergo hydrolysis reaction at room temperature overnight. In a typical synthesis, 20 g of TBT was dissolved in 20 g of ethyl alcohol with stirring for 1 hour. Then 2.12 g of acetic acid, 4.06 g of hydrochloric acid and 7 g of ethyl alcohol were mixed homogeneously and followed with adding dropwise into the above solution and stirred for another 3 hours. The obtained yellow transparent solution was allowed to undergo hydrolysis reaction at room temperature overnight.

### Synthesis of Ti–Si oxide and $TiO_2$ replica of aquatic plant leaves

The pre-fixed leaves are immersed in dilute HCl aqueous solution for 2 hours at room temperature to remove the $Mg^{2+}$ in the chlorophyll molecules. The treated samples are immersed in above as-synthesized Ti–Si oxide and $TiO_2$ precursor sol under vacuum for one day. The sol-infiltrated leaf samples were then left to dry at room temperature. The samples were then placed in muffle oven at 40, 60, 80 °C successively and tempered for two hours at each temperature, respectively. Then the samples were programmed to heat to the desired temperatures at a heating rate of 1 °C $min^{-1}$ and tempered at the temperatures for 4 hours. The nanocrystalline $TiO_2$–$SiO_2$ composite and $TiO_2$ were prepared by calcination of precursor sols at desired temperatures after hydrolyzation and drying.

### Characterization

Small pieces of fixed leaves were embedded in the tissue freezing medium (Leica Instruments Company) at −25 °C. Cross-sections of 10 μm thickness were prepared using a cryomicrotome (Leica CM3050-Cryostat, Leica Instruments Company) at −20 °C, and collected on poly(L-lysine)-coated slides. The fluorescence microscopy was carried out using Laser-Scan-Microscopy (FV1000-IX81, Olympus). Chlorophyll fluorescence was excited by 488 nm laser. The microscale morphologies of the leaves morphologies were observed using three-dimensional MicroXCT-200 (Xradia Inc. Concord) at 40 times magnification. Computed tomography (CT) facilitates viewing an object in 3D perspective. The transmission X-ray imaging of the specimen was performed using an X-ray at 90 kV, 8 W. TEM images were obtained on a JEOL JEM-2010 transmission electron microscope operating at 200 kV. Samples obtained by scratching the films from the substrate for TEM measurements were dispersed in ethanol. Carbon coated copper grids were used as the sample holder. XRD patterns were collected on a Rigaku D/MAX 2500 X-ray powder diffractometer using a high-power Cu Kα radiation.

### Photocatalytic characterization

The photocatalytic activity for methylene blue degradation was measured as follows: 100 mg of the synthesized $TiO_2$ replica sample of the leaves was dispersed in 100 mL of $10^{-5}$ mol $L^{-1}$ methylene blue aqueous solution. The suspended solution was placed in dark environment for 2 hours to reach the adsorption–desorption equilibrium. The samples were irradiated by a black light (15 W, peak wavelength: 365 nm) from a distance of 5 cm for certain minutes. The solution was sampled every certain minute and centrifuged to separate the $TiO_2$ sample. The liquid supernatant was collected and tested in Ocean Optics fiber spectrometer to measure the absorption spectra. The photodegradation experiments for each sample were performed 3 times independently and the photodegradation rate constants were averaged over 3 times. The rate of degradation was assumed to obey pseudo-first-order kinetics. The degradation rate constant, $k$ ($min^{-1}$), was obtained *via* least square fitting
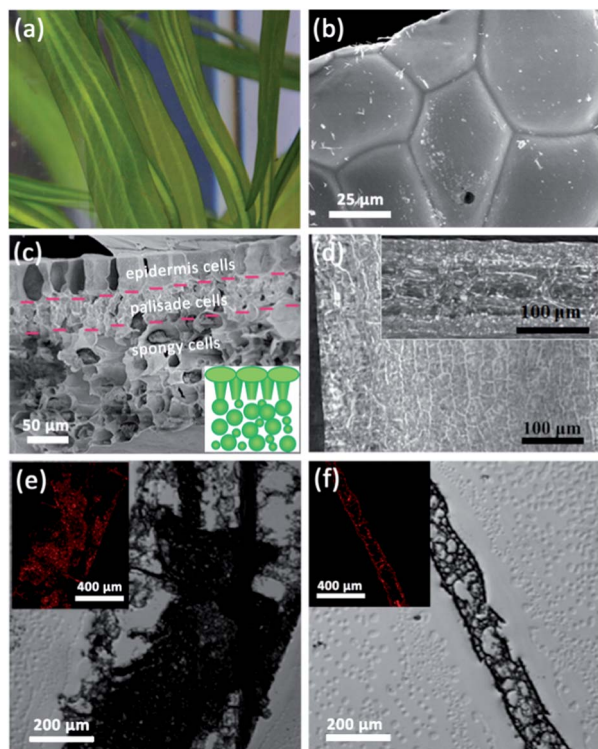
according to the equation, $A = A_0 e^{-kt}$, where $A$ was the intensity of characteristic absorption peak of MB after degradation for a time of $t$ (min), $A_0$ was the initial intensity.

## Results and discussion

The morphologies of the *Vallisneria* leaves with glutaraldehyde fixation and supercritical drying procedures were fully characterized by several techniques, including Scanning Electronic Microscopy (SEM), Transmission Electron Microscopy (TEM), confocal laser microscopy (CLSM), and Micro X-ray Computed Tomography (MicroXCT). Due to the aquatic environment, the *Vallisneria* leaves showed a large difference in morphology and structure from the terrestrial plant leaves. Underwater, the leaves seem very soft and flexible (Fig. 1a). The morphologies and internal structures of *Vallisneria* leaves were characterized anatomically (Fig. 1b–d). The results indicated that the epidermal cells showed convex lens-like shape (Fig. 1b), which was able to concentrate light into the interior of leaves for photosynthesis.[27] Moreover, the profile of the epidermal cell showed the cells with non-uniform shape and size in the range of 50–100 µm (Fig. 1c). In addition, the cross-section image demonstrated a three layer structure of epidermal layer, palisade layer and spongy layer (Fig. 1c). Specially, the thickness of
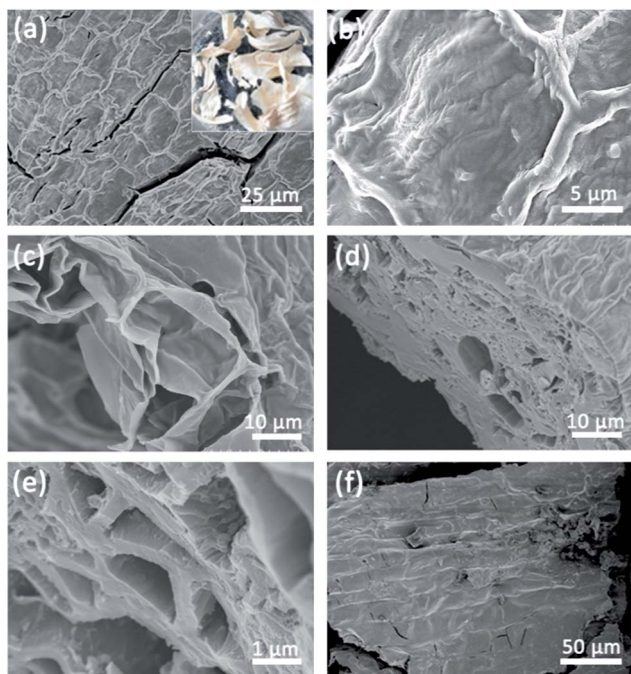


**Fig. 1** Characterization of *Vallisneria* leaves. (a) Optical image of the leaves underwater. (b) SEM images of upper epidermal cells, indicating the convex shape that can effectively concentrate the light into the interior of the leaves. (c) SEM image of cross-section of freeze-fracture leaves, indicating the clear interfaces of epidermis–palisade and palisade–sponge. The inset shows the schematic illustration of the leaf structure. (d) 3D-reconstructing image of leaves through Micro-CT. (e and f) illustrate CLSM images of the transverse and cross-section of leaves, respectively, with the inset showing the chlorophyll fluorescence in the leaves.

palisade layer was 35.5 ± 3.3 µm, accounting for 17.8% of that for the whole leaf. The ratio was smaller than that of 36.6% for palisade layer with 39.9 ± 5.5 µm thickness accounted for the thickness of *A. vitifolia* Buch. leaf reported by D. Zhang *et al.*[20] The thinner palisade layer was beneficial for the mass transport from the spongy layer with the surroundings. In addition, the spongy layer of *Vallisneria* leaf accounted for 63.9% of the thickness of the whole leaf, which was larger than the corresponding ratio of 51.7% for the spongy layer of *A. vitifolia* Buch. leaf. The spongy mesophyll cells were the primary sites to scatter and absorb light. Therefore, the aquatic leaves with more spongy mesophyll cells should have better light absorption and harvesting ability theoretically. Besides, the MicroXCT technique was employed to reconstruct the three-dimensional (3D) images of the *Vallisneria* leaf (Fig. 1d). The cross-section (inset of Fig. 1d) illustrated the internal structure of the leaf including palisade issue and chloroplasts, while the planar section showed the 2D extension of epidermal cells of the leaf. Furthermore, the cross-section and longitudinal section anatomies of the *Vallisneria* were characterized by CLSM, as illustrated in Fig. 1e and f and insets, respectively. The emitted red chlorophyll fluorescence upon 488 nm excitation indicated that the individual mesophyll cell contained a number of chloroplasts. As chloroplasts were the major sites for photosynthesis, the mesophyll cells with lots of chloroplasts were in favor of facilitating the photocatalytic performance.

The Ti–Si oxide and TiO$_2$ replicas of the aquatic leaves were synthesized by soaking the as-fixed leaves into the Ti–Si oxide and TiO$_2$ precursor sols under vacuum for 24 hours, respectively. The as-fixed leaves soaked in the sol solution ensured the sol easily penetrated into the interior of leaves and attached to the skeletons and tissues. The sol compositions and infiltration conditions played pivotal roles in the perfect replication of the leaf template. The existence of silica served the purpose of enhancing thermal stability of mesoporous structure in the Ti–Si composite. The silica glue could prevent the overgrowth of TiO$_2$ nanoparticles from destroying the mesostructures. Additionally, the silica component was conducive to the improvement of photocatalysis, especially in photocatalytic degradation of dyes due to the improved dye adsorption. After removal of dual templates by calcination, Ti–Si and TiO$_2$ replica of leaves were obtained. Interestingly, the Ti–Si-replica of *Vallisneria* (Ti–Si-rV) maintained the macroscopic morphology of the leaf templates although they could be easily squeezed into segments with external forces (insets of Fig. 2a). In addition, the microscopic morphologies of the replicas kept well in solution with long time vigorous stirring. In comparison with the TiO$_2$ replica of *Vallisneria* leaves (Ti–rV, Fig. S1†), the cell walls in Ti–Si-rV were clearer and finer, which resulted from the enhanced structural stability by SiO$_2$ addition (Fig. 2a and f). The fine structures ensured the convex shape and cavities of the epidermal cell replicas (Fig. 2b and c). Consequentially, the replicas possessed the ability to concentrate the light into the artificial leaf photocatalyst, hence improving photocatalytic capability. Compared with the leaf cells, nevertheless, the convex of the epidermal cell replicas didn't show curvatures so well, which was attributed to the limited replication ability of

**7762** | *J. Mater. Chem. A*, 2013, **1**, 7760–7766

This journal is © The Royal Society of Chemistry 2013

**Fig. 2** SEM images of Ti–Si-rV (a), epidermis cells replica (b) and its cross-section (c), cross-sections of Ti–Si-rV replica (d) and its spongy cells replica (e), as well as Ti–rV (f). In comparison, the replica of Ti–Si-rV shows more delicate structures inherited from the leaves than that of Ti–rV. The inset of (a) shows the optical image of Ti–Si-rV replicas.

the inorganics. Furthermore, the cross-section of the Ti–Si-rV indicated that the internal spongy cells were well replicated from the leaf cells (Fig. 2c and d), which could scatter and absorb the concentrated light. Accordingly, the hierarchical structured Ti–Si and TiO$_2$ replicas inherited from the leaf templates were able to facilitate the light trapping with the help of light concentration ability of the leaf cell replicas, as well as the high index ratio between TiO$_2$ and water.[31] Besides, there was another benefit from the hierarchical mesoporous materials that the mass transport during photocatalytic reaction could also be improved. Therefore, the replicas were able to facilitate the mass transport and light access, hence improving the photocatalytic capability.

A xenon lamp equipped with or without UV cut filter was separately employed as light sources to perform the photocatalytic reaction. The elements (N, C and S) in the leaves were expected to be effectively incorporated into TiO$_2$ and alter the absorbance onset of pristine TiO$_2$ driven by UV light[13] into visible light region. According to the analysis from the related XPS data and DRS spectra (Fig. S3†), the N element in the TiO$_2$ took the interstitial doping form with the binding energy of 399.4 eV, which cannot contribute to visible light activity. In addition, the photodegradation of MB under solar simulator equipped with 420 nm cut off filters in 2 hours was not obvious (Fig. S2†). The results indicated that the photocatalyst was TiO$_2$ replicas rather than visible light driven photocatalyst such as chlorophylls or N-doped TiO$_2$. Although the visible light driven photocatalyst is more important for practical applications, the photocatalyst reported herein employed the black-light lamp to perform the

photocatalytic activity characterization. The photocatalytic performances for Ti–rV replicas were firstly characterized. The photocatalytic degradation of MB aqueous solution was employed to characterize the photocatalytic activities of Ti–rV replicas. The changes of absorbance peak of MB molecule at 665 nm were monitored to evaluate the photocatalytic degradation kinetics under the black-light lamp irradiation.[32,33] The absorbance maximum of the dye molecule was blue-shifted gradually during the UV illumination due to the decomposition of the MB molecule. During the whole illumination period, the pure MB aqueous solution without adding photocatalyst as blank reference gave no decomposition (Fig. 3c). Therefore, the decomposition of MB molecules was ascribed to the TiO$_2$ photocatalysis. The absorbance spectra of MB aqueous solution were collected at specific increasing time intervals during the whole illumination process. As the crystalline phase of TiO$_2$ had a great influence on the photocatalytic performance, Firstly, the calcination temperature, one of the primary factors impacting on the crystalline phase, was considered. At the calcination temperatures of 450, 500, 600, 700 °C, all the samples showed the anatase phase (101, $2\theta = 25.4°$, Fig. 3a and b), which was the best phase for the TiO$_2$ photocatalytic performance.[34] With different calcination temperatures, the sample of Ti–rV-600 (the number denotes the calcination temperature) showed the best photocatalytic performance (Fig. 3c and d). In the range of 450 °C to 600 °C, the intensity of the anatase TiO$_2$ peak at the XRD patterns (Fig. 3b) increased with the calcination temperature increasing, which indicated the formation of anatase. The increased anatase contributed to photocatalytic capability enhancement. However, while the intensity of the anatase TiO$_2$ peak still increased. The decrease was ascribed to the crystalline size growth, which reduced the photocatalytic active sites. According to Scherrer equation: $D_c = 0.89\lambda/(B\cos\theta)$, where $D_c$ is crystalline size, $\lambda$ is the X-ray wavelength, $\theta$ is the Bragg diffraction angle, $B$ is the half
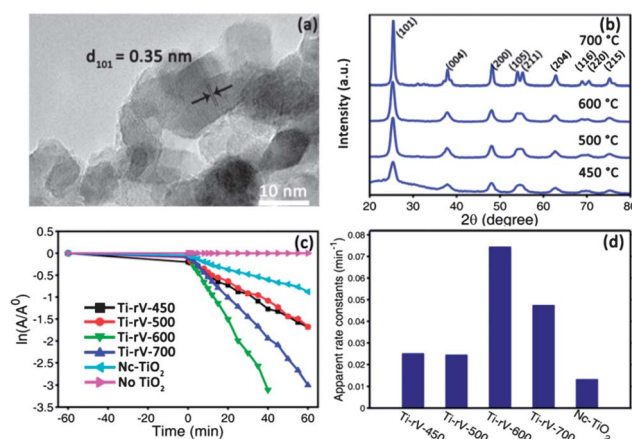


**Fig. 3** (a) HRTEM images of Ti–rV-600 under the calcination of 600 °C, which shows that the lattice distance of 0.35 nm should be assigned to anatase TiO$_2$ (101). (b) XRD characterizations under different calcination temperatures: 450 °C, 500 °C, 600 °C, 700 °C. (c and d) Reaction kinetics and their apparent rate constants of Methylene blue (MB) photodegraded by nc-TiO$_2$, blank reference, and Ti–rV under above calcination temperatures, respectively. The rate constant of Ti–rV-600 was ca. 5.6 times higher than that of nc-TiO$_2$.

width, the crystalline size is verse proportional to the half width.[35] From the XRD patterns, the half width of the (101) peak at 700 °C was smaller than that at 600 °C, which indicated that the sample calcined at 700 °C (15 nm) had larger crystalline size than the sample at 600 °C (9.9 nm, Table S1†). With the balance between crystalline phase and size, accordingly, the photocatalytic ability of Ti–rV-600 was better than other calcination temperatures. As Fig. 3d shows, the photocatalytic rate constant of Ti–rV-600 (0.0745 min$^{-1}$) is $ca.$ 5.6 times higher than that of nc-TiO$_2$ (0.0133 min$^{-1}$). The two samples had the same crystalline phase of anatase, and the surface area of Ti–rV-600 (59.7 m$^2$ g$^{-1}$) was approximately equal to that of nc-TiO$_2$ (58.5 m$^2$ g$^{-1}$). Therefore, the enhancement was devoted to the superior light harvesting ability of the leave replicas.
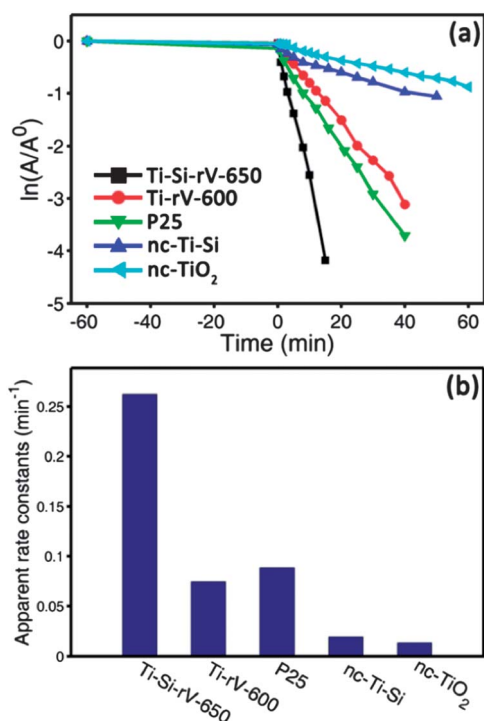
In order to further improve the photocatalytic capability, the mesoporous structure was introduced into the replica by surfactants as templates to enlarge its surface area. As illustrated in Fig. 2, the replicas of Ti–Si-rV presented clear skeleton structures in comparison with the obscure skeletons in Ti–rV replicas, due to the structure stability enhancement by the silica introduction. Moreover, the photocatalytic capability of Ti–Si-rV was characterized (Fig. 4) and showed that the rate constant (0.2622 min$^{-1}$) of Ti–Si-rV-650 (the number denotes the calcination temperature) was $ca.$ 3.5 times larger than Ti–rV-600 (0.0745 min$^{-1}$). The two samples had similar XRD patterns (Fig. 5b). Additionally, the crystalline size of Ti–Si-rV-650 (9.1 nm) approached to the size of Ti–rV-600 (9.9 nm, Table S1†).
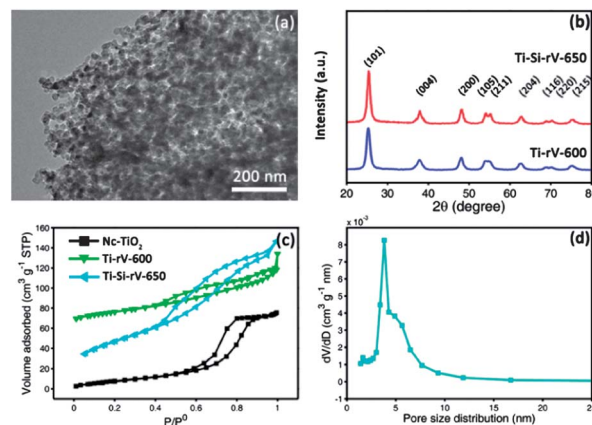


**Fig. 5** (a) HRTEM images of Ti–Si-rV under the calcination of 650 °C. (b) XRD characterizations of Ti–Si-rV-650, and Ti–rV-600. (c) N$_2$ adsorption and desorption isotherms for nc-TiO$_2$, Ti–rV-600, and Ti–Si-rV-650, respectively. (d) The pore size distribution curves for Ti–Si-rV-650. Most of the pore sizes are about 5 nm.



**Fig. 4** (a) Photocatalytic degradation kinetics of MB for Ti–Si-rV-650, Ti–rV-600, P25, nc-Ti–Si, and nc-TiO$_2$, respectively. (b) The corresponding apparent rate constants of the above samples. The rate constant of Ti–Si-rV-650 shows $ca.$ 3 times higher than that P25, $ca.$ 13.7 and $ca.$ 19.7 times higher than that of nc-Ti–Si and nc-TiO$_2$, respectively.

Therefore, it could be deduced that the enhancement resulted from the larger surface area and better light harvesting capability for Ti–Si-rV-650 than Ti–rV-600. With the p123 as a template, the nanoparticles (6–10 nm) in Ti–Si-rV-650 formed a dense and continuous film with wormlike mesopores (Fig. 5a). The pore sizes were approximately 5 nm (Fig. 5d). Furthermore, the silica particles were observed to exist in the skirt of TiO$_2$ nanocrystals due to the non-crystallized property of silica under the adopted calcination conditions. In order to measure the surface area of Ti–Si-rV-650 and Ti–rV-600, the N$_2$ adsorption–desorption experiment was conducted. The result indicated that the two samples had the same isotherms of type IV, suggesting the presence of mesopores. The shapes of the hysteresis loops for the Ti–Si-rV-650 was of type H3, which was assigned to slit-like pores generated by the aggregations of the plate-like particles (Fig. 5c). With calculation, the surface area of Ti–Si-rV-650 (167.1 m$^2$ g$^{-1}$) was $ca.$ 2.8 times larger than that of Ti–rV-600 (59.7 m$^2$ g$^{-1}$). The surface area should be the primary factor devoting to the photocatalytic performance enhancement. Another factor for the contribution was attributed to the thin and fine mimicked replica structures. The thin hierarchical replicas were able to easily access light and had excellent mass transport and dye adsorption capability. In addition, the finer mimicked replicas structures had better light concentration and absorption ability for Ti–Si-rV-650 than its Ti–rV-600 counterpart (Fig. 2a and f). For these reasons, the photocatalytic performance of Ti–Si-rV-650 was much better than that of Ti–rV-600.

Both Ti–Si-rV-650 and Ti–rV-600 were artificial leaves, which inherited the light concentration and scattering capability of the natural leaves. In order to further illustrate the inherited light harvesting ability of the replicas, the photocatalytic performance of Ti–Si-rV-650 was characterized and compared with its nc-Ti–Si and nc-TiO$_2$ counterparts (Fig. 4). As the only difference between Ti–Si-rV-650 and nc-Ti–Si was the structure of leaf template, the rate constant of Ti–Si-rV-650 (0.2622 min$^{-1}$) was $ca.$ 13.7 times larger than nc-Ti–Si (0.0191 min$^{-1}$). The result strongly indicated the superior light harvesting ability of

the replicas. In addition, the rate constant of Ti–Si-rV-650 (0.2622 min$^{-1}$) was *ca.* 19.7 times larger than nc-TiO$_2$ (0.0133 min$^{-1}$), and even *ca.* 3 times larger than Degussa P25 (0.0884 min$^{-1}$), which is the best commercial TiO$_2$ photocatalytic material.[36] Although with same crystalline phase (Fig. 5b), the crystalline size of Ti–Si-rV-650 (9.1 nm) was smaller than nc-TiO$_2$ (15.1 nm). Additionally, the surface area of Ti–Si-rV-650 (167.1 m$^2$ g$^{-1}$) was 2.86 times larger than that of nc-TiO$_2$ (58.5 m$^2$ g$^{-1}$). The large surface area of Ti–Si-rV-650 is one of the primary reasons for the performance enhancement. On the other hand, the structural element should be considered as another primary reason. The hierarchical bio-templated artificial leaves not only had high surface area to provide with more active photocatalytic sites but also concentrated the incident light by the epidermal cells and efficiently scattered the focused light by the spongy cells to prolong the light path. In addition, the thin leave replicas were in favor of accessing the light so that the light could be utilized efficiently, as well as promoting the mass transportation to accelerate the photocatalytic reaction. The synergetic effect made the hierarchical artificial leaves possess outstanding photocatalytic capability. Therefore, the artificial leaves inherited the light concentration and harvesting ability of the natural leaves.

## Conclusion

To sum up, the full potential of the aquatic leaf in constructing TiO$_2$ based artificial leaves was exploited in combination with a mesoporous directing agent. Under the optimized conditions, the Ti–Si-rV-600 showed 3.0 times higher than P25 and 19.7 times higher than ordinary nanocrystalline TiO$_2$ in photodegradation of MB under UV irradiation. The obtained materials inherited the hierarchical structures of aquatic plants and high surface area of mesoporous template. The excellent photocatalytic properties of the as-synthesized Ti–Si and TiO$_2$ photocatalyst were verified by the photocatalytic degradation of MB. The accurate replication of the aquatic plant leaves ensured the obtained photocatalyst with optimal structure for light harvesting, while the introduction of P123 as mesoporous template offset the loss of intricate structures of biological templates in the final replica. The work reported here provided a feasible and effective solution to synthesize bioinspired hierarchical systems for high efficiency photocatalysis. The work can be easily extended to other semiconductor photocatalysts and will be promising for the future related research. Further work on artificial construction of the light harvesting structure is under investigation.

## Acknowledgements

## Notes and references

1 O. K. Varghese, M. Paulose, T. J. LaTempa and C. A. Grimes, *Nano Lett.*, 2009, **9**, 731–737.

2 X. Wang, K. Maeda, A. Thomas, K. Takanabe, G. Xin, J. M. Carlsson, K. Domen and M. Antonietti, *Nat. Mater.*, 2009, **8**, 76–80.

3 X. Wang, G. Liu, L. Wang, Z.-G. Chen, G. Q. Lu and H.-M. Cheng, *Adv. Energy Mater.*, 2012, **2**, 42–46.

4 T. Y. Peng, D. Zhao, K. Dai, W. Shi and K. Hirao, *J. Phys. Chem. B*, 2005, **109**, 4947–4952.

5 A. A. Ismail and D. W. Bahnemann, *J. Mater. Chem.*, 2011, **21**, 11686–11707.

6 X. Wang, Q. Xu, M. Li, S. Shen, X. Wang, Y. Wang, Z. Feng, J. Shi, H. Han and C. Li, *Angew. Chem., Int. Ed.*, 2012, **51**, 13089–13092.

7 X. X. Xu, C. Randorn, P. Efstathiou and J. T. S. Irvine, *Nat. Mater.*, 2012, **11**, 595–598.

8 M.-C. Wu, J. Hiltunen, A. Sapi, A. Avila, W. Larsson, H.-C. Liao, M. Huuhtanen, G. Toth, A. Shchukarev, N. Laufer, A. Kukovecz, Z. Konya, J.-P. Mikkola, R. Keiski, W.-F. Su, Y.-F. Chen, H. Jantunen, P. M. Ajayan, R. Vajtai and K. Kordas, *ACS Nano*, 2011, **5**, 5025–5030.

9 S. Yu, H. J. Yun, D. M. Lee and J. Yi, *J. Mater. Chem.*, 2012, **22**, 12629–12635.

10 D. J. Yang, C. C. Chen, Z. F. Zheng, H. W. Liu, E. R. Waclawik, Z. M. Yan, Y. N. Huang, H. J. Zhang, J. C. Zhao and H. Y. Zhu, *Energy Environ. Sci.*, 2011, **4**, 2279–2287.

11 H. G. Yu, H. Irie and K. Hashimoto, *J. Am. Chem. Soc.*, 2010, **132**, 6898–6899.

12 J. Zhuang, Q. Tian, H. Zhou, Q. Liu, P. Liu and H. Zhong, *J. Mater. Chem.*, 2012, **22**, 7036–7042.

13 J. Liu, M. Li, J. Wang, Y. Song, L. Jiang, T. Murakami and A. Fujishima, *Environ. Sci. Technol.*, 2009, **43**, 9425–9431.

14 X. Li, T. Fan, H. Zhou, S.-K. Chow, W. Zhang, D. Zhang, Q. Guo and H. Ogawa, *Adv. Funct. Mater.*, 2009, **19**, 45–56.

15 X.-D. Gao, X.-M. Li, X.-Y. Gan, Y.-Q. Wu, R.-K. Zheng, C.-L. Wang, Z.-Y. Gu and P. He, *J. Mater. Chem.*, 2012, **22**, 18930–18938.

16 Q. Yang, M. Li, J. Liu, W. Shen, C. Ye, X. Shi, L. Jiang and Y. Song, *J. Mater. Chem. A*, 2013, **1**, 541–547.

17 Y. Lu, H. Yu, S. Chen, X. Quan and H. Zhao, *Environ. Sci. Technol.*, 2012, **46**, 1724–1730.

18 J. Liu, G. Liu, M. Li, W. Shen, Z. Liu, J. Wang, J. Zhao, L. Jiang and Y. Song, *Energy Environ. Sci.*, 2010, **3**, 1503–1506.

19 N. Shi, X. Li, T. Fan, H. Zhou, J. Ding, D. Zhang and H. Zhu, *Energy Environ. Sci.*, 2011, **4**, 172–180.

20 H. Zhou, X. F. Li, T. X. Fan, F. E. Osterloh, J. Ding, E. M. Sabio, D. Zhang and Q. X. Guo, *Adv. Mater.*, 2010, **22**, 951–956.

21 S. Bensaid, G. Centi, E. Garrone, S. Perathoner and G. Saracco, *ChemSusChem*, 2012, **5**, 500–521.

22 G. A. Ozin, J. I. L. Chen, E. Loso and N. Ebrahim, *J. Am. Chem. Soc.*, 2008, **130**, 5420–5421.

23 J. I. L. Chen, G. von Freymann, S. Y. Choi, V. Kitaev and G. A. Ozin, *Adv. Mater.*, 2006, **18**, 1915–1919.

This journal is © The Royal Society of Chemistry 2013

*J. Mater. Chem. A*, 2013, **1**, 7760–7766 | **7765**

24 H. Zhou, T. Fan, X. Li, D. Zhang, Q. Guo and H. Ogawa, *J. Mater. Chem.*, 2009, **19**, 2695–2703.

25 P. G. Falkowski and J. A. Raven, *Aquatic photosynthesis*, Blackwell Science, Malden, MA, 1997.

26 J. T. O. Kirk, *Light and Photosynthesis in Aquatic Ecosystems*, Cambridge University Press, 2011.

27 T. C. Vogelmann, *Annu. Rev. Plant Physiol. Plant Mol. Biol.*, 1993, **44**, 231–251.

28 Z. Xie, E. J. Henderson, O. Dag, W. Wang, J. E. Lofgreen, C. Kübel, T. Scherer, P. M. Brodersen, Z. Z. Gu and G. A. Ozin, *J. Am. Chem. Soc.*, 2011, **133**, 5094–5102.

29 W. Y. Dong, Y. J. Sun, C. W. Lee, W. M. Hua, X. C. Lu, Y. F. Shi, S. C. Zhang, J. M. Chen and D. Y. Zhao, *J. Am. Chem. Soc.*, 2007, **129**, 13894–13904.

30 X. Fu, L. A. Clark, Q. Yang and M. A. Anderson, *Environ. Sci. Technol.*, 1996, **30**, 647–653.

31 Y. Zhao, X. T. Zhang, J. Zhai, J. L. He, L. Jiang, Z. Y. Liu, S. Nishimoto, T. Murakami, A. Fujishima and D. B. Zhu, *Appl. Catal., B*, 2008, **83**, 24–29.

32 J. S. Lee, K. H. You and C. B. Park, *Adv. Mater.*, 2012, **24**, 1084–1088.

33 C. An, S. Peng and Y. Sun, *Adv. Mater.*, 2010, **22**, 2570–2574.

34 J. Ovenstone and K. Yanagisawa, *Chem. Mater.*, 1999, **11**, 2770–2774.

35 X. Xue, W. Ji, Z. Mao, H. Mao, Y. Wang, X. Wang, W. Ruan, B. Zhao and J. R. Lombardi, *J. Phys. Chem. C*, 2012, **116**, 8792–8797.

36 S. M. Zhu, D. Zhang, Z. X. Chen, G. Zhou, H. B. Jiang and J. L. Li, *J. Nanopart. Res.*, 2010, **12**, 2445–2456.